

A radio transient with unusually slow periodic emission

N. Hurley-Walker^{*1}, X. Zhang^{2,3}, A. Bahramian¹, S. J. McSweeney¹, T. N. O’Doherty¹, P. J. Hancock¹,
J. S. Morgan¹, G. E. Anderson¹, G. H. Heald², T. J. Galvin¹

¹*International Centre for Radio Astronomy Research, Curtin University, Kent St, Bentley WA 6102, Australia*

²*CSIRO, Space and Astronomy, PO Box 1130, Bentley WA 6102, Australia*

³*Shanghai Astronomical Observatory, Chinese Academy of Sciences, 80 Nandan Road, Shanghai 200030, China*

The high-frequency radio sky is bursting with synchrotron transients from massive stellar explosions and accretion events, but the low-frequency radio sky has so far been quiet beyond the Galactic pulsar population and the long-term scintillation of AGN. The low-frequency band, however, is sensitive to exotic coherent and polarised radio emission processes such as electron cyclotron maser emission from flaring M-dwarfs¹, stellar magnetospheric plasma interactions with exoplanets², and a population of steep-spectrum pulsars³, making Galactic plane searches a prospect for blind transient discovery. Here we report an analysis of archival low-frequency radio data that reveals a periodic, low-frequency radio transient. We find that the source pulses every 18.18 minutes, an unusual periodicity not previously observed. The emission is highly linearly polarised, bright, persists for 30–60 s on each occurrence, and is visible across a broad frequency range. At times the pulses comprise short (< 0.5 -s) duration bursts; at others, a smoother profile is observed. These profiles evolve on timescales

of hours. By measuring the dispersion of the radio pulses with respect to frequency, we have localised the source to within our own Galaxy, and suggest that it could be an ultra-long period magnetar.

We searched 24 hours of Galactic Plane observations taken by the Murchison Widefield Array (MWA; see Methods) using a rapid shallow search method to probe a novel transient timescale parameter space (Hancock et al. in prep). From this search, we discovered the transient source GLEAM-X J 162759.5-523504.3, initially with two significant detections. An exhaustive further search yielded 71 pulses spanning January to March 2018 (Fig. 1), with maximum flux densities ranging from 5–40 Jy (Fig. 2). The pulse widths range between 30 and 60 s, and evolve on hourly timescales, sometimes comprising many “spiky” bursts unresolved at our time resolution of 0.5 s, other times displaying sub-pulses of widths 10–30 s. Aligning the pulses, we established a period of 1091.1690 ± 0.0005 seconds (see Methods). It was necessary to perform a barycentric correction, indicating an extrasolar origin.

Using data spanning 72–231 MHz, we established a dispersion measure of 57 ± 1 pc cm⁻³ (see Methods; Extended Data Fig. 1), which when combined with Galactic electron density models⁵, produces a distance estimate of 1.3 ± 0.5 kpc. We also measured a radio spectral index of $\alpha = -1.16 \pm 0.04$, where the flux density $S_\nu \propto \nu^\alpha$, indicating that the emission is non-thermal. Brightness variations on timescales of less than 0.5 s imply a compact object, and the brightness temperature of a thermal object 0.5 light seconds in size producing 20 Jy of flux density at 1.3 kpc is $\approx 10^{16}$ K, implying a coherent emission mechanism.

The pulses exhibit a constant, high fractional linear polarisation ($88 \pm 1\%$) and there is no change in polarisation angle as either a function of pulse phase or observation time (Fig. 3). The Faraday rotation measure (RM) remains constant over the observations at $-61 \pm 1 \text{ rad m}^{-2}$, which is consistent with the Galactic RM towards this region⁶ ($-72.3 \pm 154.9 \text{ rad m}^{-2}$).

The fluence of the pulses is variable but broadly follows a distribution with two “on” intervals ~ 30 days wide (Jan 03 – Feb 02 and Feb 28 – Mar 28: see Fig. 2), with fast rise times, slow decay times, and a 26-day null interval between them. The detections are all serendipitous in archival data, leading to heterogeneous coverage. During the “on” intervals, at every time where we predict we would detect a pulse, we do so (i.e. there is no obvious nulling). The flux density in 30-s images at the source location is $< 10 \text{ mJy}$ during the sampled “off” intervals (upper limits in Fig. 2). While the fluence variation does somewhat resemble gravitational lensing⁷ or extreme scattering events⁸, the magnification required would be of order $1,000\times$, and difficult to create with any physically plausible gravitational or plasma lens.

The high linear polarisation indicates the presence of strongly ordered magnetic fields; this and the luminosity of the pulses are not explicable by known phenomena such as radio emission from flare stars⁹, exoplanets¹⁰, and white dwarf/m-dwarf binaries¹¹, all of which would be orders of magnitude fainter at this distance, and typically circularly polarised. The extreme regularity of the emission (fractional uncertainty $\frac{\sigma_P}{P} < 5 \times 10^{-7}$) implies either a rotational or orbital origin. Due to the 0.5 light-second upper limit on the object’s size, a rotational origin may be more likely.

Fig. 4 shows GLEAM-X J162759.5-523504.3 in context with other sources of transient

emission. The source that bears the most similarity to GLEAM-X J 162759.5-523504.3 is GCRT 1745, a transient radio source detected toward the Galactic Centre with observations at 330 MHz, which exhibited five 10-minute duration bursts with periodicity 77 min¹². These bursts exhibited slow profile evolution and low circular polarisation (no linear polarisation measurements were available). Due to the crowded field in this direction, and lack of distance constraints, Hyman et al. were unable to determine a progenitor but speculated that it may be a long-period magnetar, an interpretation that can be applied to GLEAM-X J 162759.5-523504.3.

Magnetic neutron stars rotating at period P lose energy via magnetic dipole radiation, causing them to spin down (i.e. they have a positive period derivative \dot{P}); this spin down luminosity (\dot{E}) can be expressed as $\frac{4\pi I \dot{P}}{P^3}$, where I is the neutron star moment of inertia, typically assumed to be 10^{45} g cm⁻². Via a grid search for P and \dot{P} (see Methods), we find that $\dot{P} > 0$ is preferred, the best fit value is $\dot{P} = 6 \times 10^{-10}$ s s⁻¹, the analysis favours $\dot{P} < 1.2 \times 10^{-9}$ s s⁻¹ (see Extended Data Fig. 7 for context with known neutron stars). Using this value as an upper limit, we find a maximum spin-down luminosity of $\dot{E} < 1.2 \times 10^{28}$ erg s⁻¹. The flux density of radio pulsars can be converted to a luminosity (see Methods) which for the brightest pulses from GLEAM-X J 162759.5-523504.3 is 4×10^{31} erg s⁻¹. Pulsar radio luminosities are typically a small fraction of their spin-down luminosities¹³, while this source exhibits the reverse, indicating that the emission is not generated purely by spin-down. Additionally, the smooth variations in pulse profile and the transient window of radio emission are more consistent with the interpretation of GLEAM-X J 162759.5-523504.3 as a radio magnetar than a pulsar¹⁴.

Magnetars are commonly detected and characterised via X-ray observations; four of the five known magnetars that have produced detectable pulsed radio emission have done so only after X-ray outbursts. However, not all X-ray emitting magnetars produce detectable radio emission. Previous studies have shown that magnetars only produce radio emission if their quiescent X-ray luminosity in the 0.5–10 keV band is lower than their spin-down luminosity¹⁵. We would therefore predict that the X-ray luminosity L_X of GLEAM-X J 162759.5-523504.3 is $< 6 \times 10^{27} \text{ erg s}^{-1}$. We obtained X-ray observations with the *Swift*/XRT and determined that $L_X < 10^{32} \text{ erg s}^{-1}$ (see Methods), which while not a strong limit compared to our expectation under this interpretation, is a lower quiescent X-ray luminosity than all but two of the faintest known magnetars¹⁶, SGR 0418 + 5729 and Swift J 1822.3 – 1606. Alternatively, a white dwarf would have a moment of inertia and therefore spin-down luminosity $10^5 \times$ larger, allowing the possibility of spin-powered radio pulsations; deeper UV observations than currently available would test this hypothesis.

Regardless of interpretation, the existence of an unexpected slowly pulsating, yet intermittent radio transient opens up an entirely new field of exploration of radio surveys, particularly at low frequencies. While many sensitive low-frequency ($\lesssim 340 \text{ MHz}$) continuum surveys have searched for transients on cadences of minutes within extragalactic fields for up to an hour at a time, no such systematic survey for unknown minute-period transients has been conducted within the Galactic plane on similar timescales^{17–21}. Since known pulsars and magnetars have periods of $\lesssim 10 \text{ s}$, surveys are typically designed with relatively short dwell times of $\approx 100\text{--}5000 \text{ s}$ ²² and employ high pass filters to mitigate red telescope noise²³, rendering them insensitive to long-period sources. Current MWA survey strategies^{20,24} may therefore be sensitive to a large population of

these sources and further detections may explain some of the other puzzling unidentified low-frequency Galactic transients¹².

We can estimate the population of similar long-period transients detectable with future searches starting from the following assumptions: like other first detections of a new class of object, GLEAM-X J 162759.5-523504.3 is the most luminous example of its kind; the population's luminosity and spatial distribution are similar to that of pulsars; other sources would have similar long-term duty cycles of $\approx 2\%$ (see Methods). Now that we are aware of this class of objects, it is worth the computational expense of performing model-subtracting time-step imaging (see Methods), and searching all voxels for significant residuals, a technique $10\times$ more sensitive than the fast search that detected GLEAM-X J 162759.5-523504.3 (see diagonal magenta lines in Fig. 4). With these population assumptions, and using this technique, we predict ≈ 10 further detections of similar objects in the same volume of data that yielded GLEAM-X J 162759.5-523504.3 (24 hours). Larger duty cycles or a flatter luminosity distribution would increase this number. The MWA archive contains thousands of hours of observing time sensitive to $|b| < 10^\circ$, which may potentially yield hundreds of further similar objects; this will also be true of other radio archives with data covering the Galactic Plane. Further detections and rapid high-time-resolution follow-up of candidates will more conclusively determine the nature of these sources, thus providing further insight into the evolutionary extremes surrounding the life and death of massive stars.

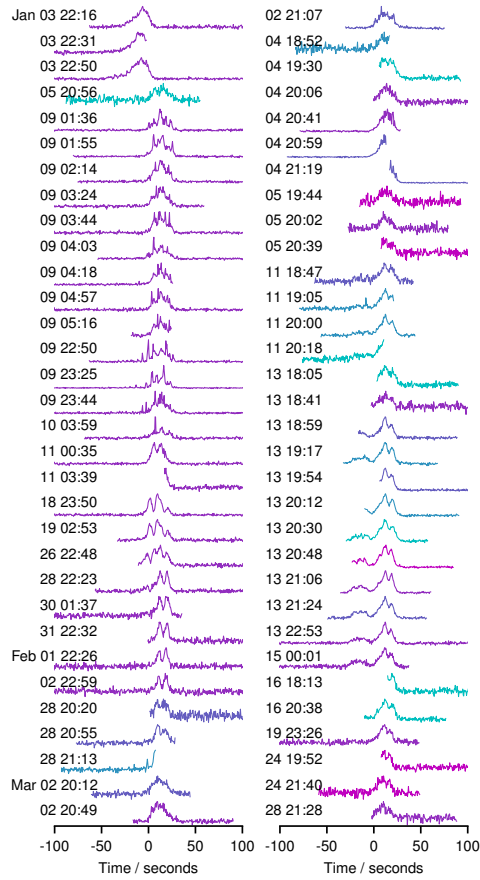


Figure 1: 64 of the 71 detected pulses of GLEAM-X J 162759.5-523504.3 aligned by its measured period P and period derivative \dot{P} . Omitted pulses were truncated or too low in signal-to-noise to be displayed here; flux densities are normalised to the peak of each pulse for readability; barycentric and dispersive corrections have been applied. The observation start times in UTC are listed on the left of each detection. The color range spans 88 MHz (cyan) to 215 MHz (magenta) and the detections span 84 days. The pulses observed on Jan 03 are not misaligned and fit within the widest pulse windows found in Mar 13 (see Methods).

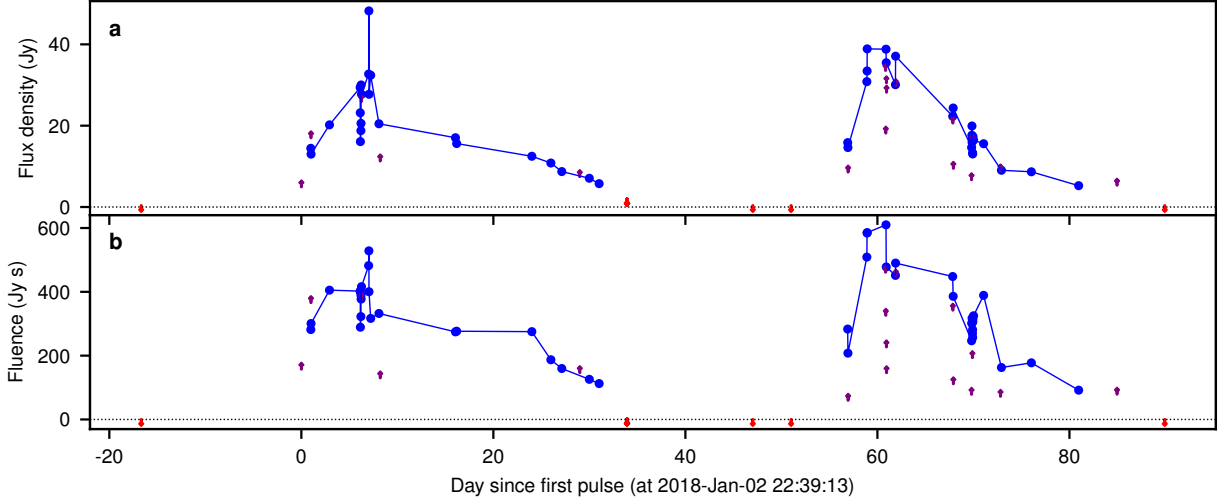


Figure 2: Maximum brightness of each pulse (a) and total pulse fluence (b) as a function of time across the two observed intervals of activity. Not all pulses are fully captured by every observation; in these cases lower limits are plotted with purple upward-pointing arrows. Observations in which the source was within the field-of-view and predicted to be detectable, but not found, are shown with red downward-pointing arrows equal to the root-mean-square noise in a 30-s image corresponding to the time we would have expected a pulse. All measurements have been scaled to a common frequency of 154 MHz via the spectral index $\alpha = -1.16$. Error bars are omitted for clarity, and are dominated by the $\sim 5\%$ uncertainty in the primary beam model of the telescope.

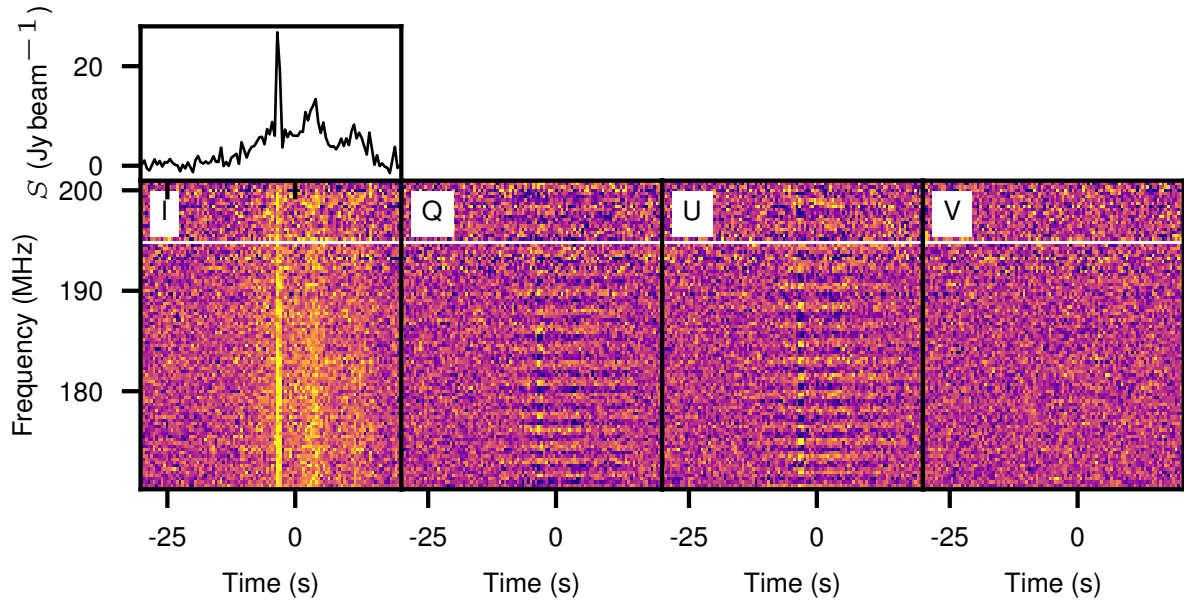


Figure 3: Dynamic spectrum of the observation recorded at 2018-01-10 03:59. From left to right the panels show the Stokes I, Q, U, and V flux density as a function of frequency and time, with a dispersion correction of 57 pc cm^{-3} applied. Linear Stokes Q and U show Faraday rotation of $-61 \pm 1 \text{ rad m}^{-2}$ while circular V shows no obvious signal. The top left panel of the image shows the profile of the Stokes I data averaged over the frequency axis; the unresolved burst of emission shows the limitation of our 0.5 s time resolution. The root-mean-square of the noise in each spectrum is 8.5 Jy beam^{-1} , and 0.9 Jy beam^{-1} in the summed profile.

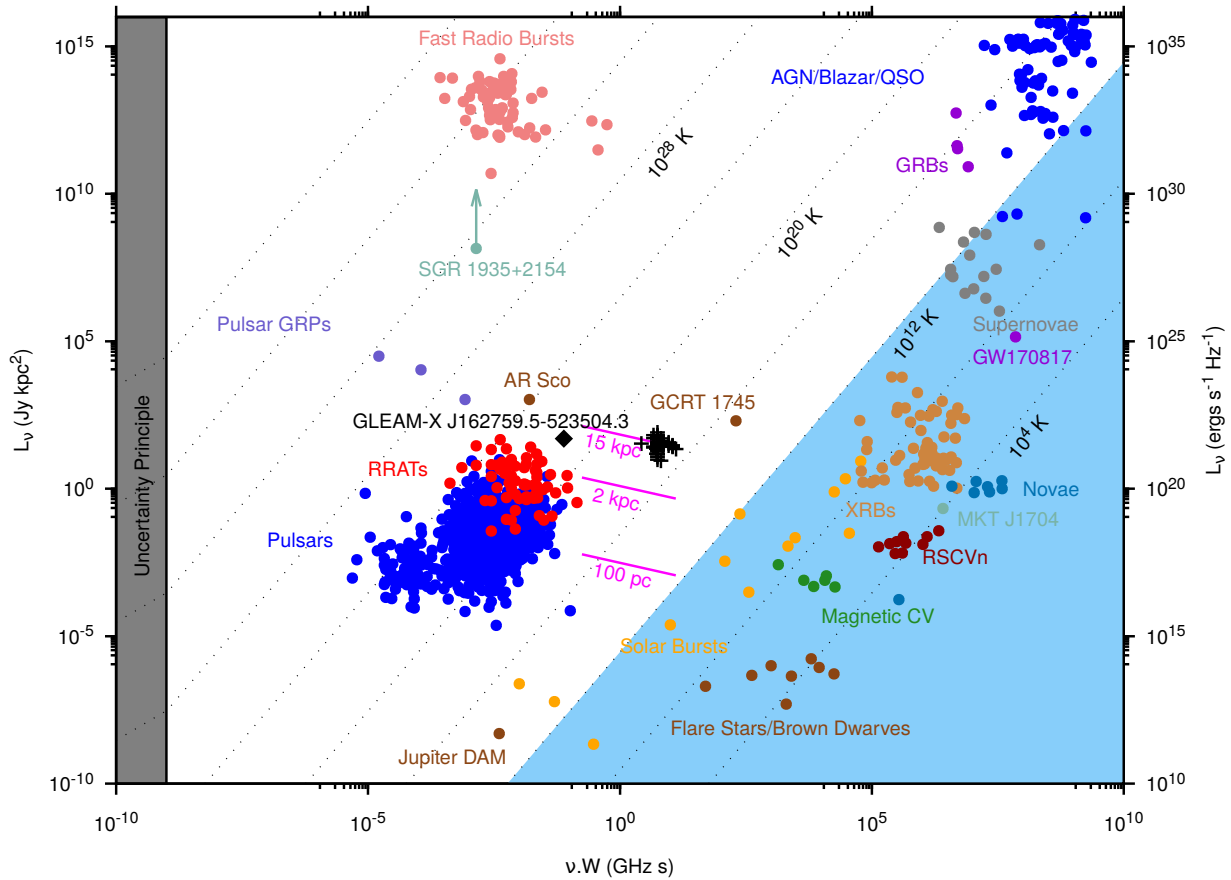


Figure 4: Transient parameter space populated with common known radio transients. Radio pseudo-luminosity is shown on the vertical axis and the product of observing frequency ν and transient/variability timescale W is plotted on the horizontal axis. The shaded blue region shows objects with brightness temperatures that do not imply coherent emission mechanisms. Black “+” marks show the $W = 30\text{--}60\text{-s}$ pulses of GLEAM-X J 162759.5-523504.3, while a black filled diamond indicates a representative unresolved pulse of $W = 0.5\text{ s}$ and $S = 30\text{ Jy}$. Diagonal magenta lines show the sensitivity of the MWA to long-pulse transients at Galactic distances, for $W = 2\text{--}60\text{ s}$ across 72–231 MHz, with dispersion measure smearing effects included. This figure is adapted from Pietka et al. 2015⁴.

1. Lynch, C. R., Lenc, E., Kaplan, D. L., Murphy, T. & Anderson, G. E. 154 MHz Detection of Faint, Polarized Flares from UV Ceti. *Astrophys. J. Lett.* **836**, L30 (2017).
2. Vedantham, H. K. *et al.* Coherent radio emission from a quiescent red dwarf indicative of star-planet interaction. *Nature Astronomy* **4**, 577–583 (2020).
3. Swainston, N. A. *et al.* Discovery of a Steep-spectrum Low-luminosity Pulsar with the Murchison Widefield Array. *Astrophys. J. Lett.* **911**, L26 (2021).
4. Pietka, M., Fender, R. P. & Keane, E. F. The variability time-scales and brightness temperatures of radio flares from stars to supermassive black holes. *Mon. Not. R. Astron. Soc.* **446**, 3687–3696 (2015).
5. Yao, J. M., Manchester, R. N. & Wang, N. A New Electron-density Model for Estimation of Pulsar and FRB Distances. *Astrophys. J.* **835**, 29 (2017).
6. Hutschenreuter, S. & Enßlin, T. A. The Galactic Faraday depth sky revisited. *Astron. & Astrophys.* **633**, A150 (2020).
7. Vedantham, H. K. *et al.* Symmetric Achromatic Variability in Active Galaxies: A Powerful New Gravitational Lensing Probe? *Astrophys. J.* **845**, 89 (2017).
8. Bannister, K. W. *et al.* Real-time detection of an extreme scattering event: Constraints on Galactic plasma lenses. *Science* **351**, 354–356 (2016).
9. Benz, A. O. & Güdel, M. Physical Processes in Magnetically Driven Flares on the Sun, Stars, and Young Stellar Objects. *Ann. Rev. Astron. Astrophys.* **48**, 241–287 (2010).

10. Zarka, P., Treumann, R. A., Ryabov, B. P. & Ryabov, V. B. Magnetically-Driven Planetary Radio Emissions and Application to Extrasolar Planets. *Astrophys. Space Sci.* **277**, 293–300 (2001).
11. Marsh, T. R. *et al.* A radio-pulsing white dwarf binary star. *Nature* **537**, 374–377 (2016).
12. Hyman, S. D. *et al.* A powerful bursting radio source towards the Galactic Centre. *Nature* **434**, 50–52 (2005).
13. Szary, A., Zhang, B., Melikidze, G. I., Gil, J. & Xu, R.-X. Radio Efficiency of Pulsars. *Astrophys. J.* **784**, 59 (2014).
14. Levin, L. *et al.* Radio emission evolution, polarimetry and multifrequency single pulse analysis of the radio magnetar PSR J1622-4950. *Mon. Not. R. Astron. Soc.* **422**, 2489–2500 (2012).
15. Rea, N., Pons, J. A., Torres, D. F. & Turolla, R. The Fundamental Plane for Radio Magnetars. *Astrophys. J. Lett.* **748**, L12 (2012).
16. Olausen, S. A. & Kaspi, V. M. The McGill Magnetar Catalog. *Astrophys. J. Suppl.* **212**, 6 (2014).
17. Carbone, D. *et al.* New methods to constrain the radio transient rate: results from a survey of four fields with LOFAR. *Mon. Not. R. Astron. Soc.* **459**, 3161–3174 (2016).
18. Polisensky, E. *et al.* Exploring the Transient Radio Sky with VLITE: Early Results. *Astrophys. J.* **832**, 60 (2016).

19. Stewart, A. J. *et al.* LOFAR MSSS: detection of a low-frequency radio transient in 400 h of monitoring of the North Celestial Pole. *Mon. Not. R. Astron. Soc.* **456**, 2321–2342 (2016).
20. Bell, M. E. *et al.* The Murchison Widefield Array Transients Survey (MWATS). A search for low-frequency variability in a bright Southern hemisphere sample. *Mon. Not. R. Astron. Soc.* **482**, 2484–2501 (2019).
21. Hajela, A., Mooley, K. P., Intema, H. T. & Frail, D. A. A GMRT 150 MHz search for variables and transients in Stripe 82. *Mon. Not. R. Astron. Soc.* **490**, 4898–4906 (2019).
22. Keith, M. J. *et al.* The High Time Resolution Universe Pulsar Survey – I. System configuration and initial discoveries. *Mon. Not. R. Astron. Soc.* **409**, 619–627 (2010).
23. Cameron, A. D., Barr, E. D., Champion, D. J., Kramer, M. & Zhu, W. W. An investigation of pulsar searching techniques with the fast folding algorithm. *Mon. Not. R. Astron. Soc.* **468**, 1994–2010 (2017).
24. Hurley-Walker, N. *et al.* GaLactic and Extragalactic All-sky Murchison Widefield Array (GLEAM) survey - I. A low-frequency extragalactic catalogue. *Mon. Not. R. Astron. Soc.* **464**, 1146–1167 (2017).

Methods

Observations The Murchison Widefield Array is a low-frequency radio telescope operating in the Murchison region of Western Australia^{25,26}. At the time of the observation in which GLEAM-XJ 162759.5-523504.3 was discovered, it was engaged in observing the GaLactic and Extragalac-

tic All-sky MWA – eXtended (GLEAM-X) survey, a follow-up to the GLEAM survey²⁷. The data were taken in a drift scan mode, iterating through a 72–231 MHz bandwidth by dwelling for 2 minutes in each of five 30.72-MHz bands, yielding a resolution of $5'–45''$ and snapshot noise levels of $150–25 \text{ mJy beam}^{-1}$. Over this bandwidth the field-of-view of the instrument is $60^\circ–25^\circ$ across, yielding multiple measurements of sources drifting through the primary beam. The data are sampled at 0.5-s time resolution and 10-kHz frequency resolution. We downloaded measurement sets from the MWA All-Sky Virtual Observatory (<https://asvo.mwatelescope.org/>) and at this stage averaged the data to 40 kHz to reduce data size and decrease processing times.

The initial detection of the transient was made by performing a differencing of the visibilities between observations taken at an identical Local Sidereal Time several months apart (Hancock et al. in prep). Two detections were made, and based on the non-detections in adjacent observations, an initial period was determined. Including a barycentric correction, and searching the archive thoroughly between July 2017 and July 2018, the interval of activity was established to be January 2018 to March 2018, with a total of 71 detections (see Supplementary Methods for further details on searching the MWA archive).

Calibration and imaging For all data, calibration was performed using the MITHCAL algorithm²⁸ to derive antenna gains by comparing the raw data to model visibilities formed from a sky model based on catalogues derived from GLEAM^{24,29}. These were applied to the observation, and deep imaging was subsequently performed using WSCLEAN³⁰ version 2.9.0, creating a visibility model that includes the spectrally variant primary beam. A $10' \times 10'$ region around GLEAM-X J 162759.5-523504.3 was masked during this process, so that the source is not included in the model.

After the deep model was created and subtracted from the visibilities, the data were re-imaged such that the transient was the only source in the field. The data were imaged at 320 kHz frequency resolution and 0.5 s time resolution in full Stokes (I,Q,U,V), which were formed from the instrumental data by application of the MWA beam model³¹. We also used observations of a polarisation calibrator (PKS J0636–2036) to correct radio emission leaking from Stokes U into Stokes V (X-Y phase calibration³²).

Dispersion Measure Since strong pulse profile evolution is observed, we used the five observations that spanned 72–231 MHz in the shortest interval of time (74 minutes; Extended Data Fig. 1) to calculate the dispersion measure. We aligned these observations using a period of 1091.1690 s, then ran dedispersion trials in steps of 0.5 over range 50 to 60 pc cm⁻³, finding that 57 ± 1 pc cm⁻³ produced the best fit. Light curves (Fig. 1) were then produced for each observation by applying dedispersion and averaging the dynamic spectra along the frequency axis.

Polarisation Polarisation analysis was performed following the methods of the Polarised GLEAM Survey (POGS^{33,34}). From all observations with detections, only observations within 170–230 MHz were selected for the polarisation analysis to avoid depolarisation caused by the (40 kHz) channel width. We performed RM synthesis³⁵ on the time-averaged Q/U spectrum of each observation with the RM Tools software (<https://github.com/CIRADA-Tools/RM-Tools>) to obtain the corresponding RM, fractional polarisation, and polarisation angle (see Fig. 6 for these results in context with the surrounding region of sky). To investigate any variation of the polarisation angle within the pulse phase, we also performed RM synthesis on the Q/U spectrum of each timestep for two high S/N observations. We found that the polarisation angle was constant with respect to time

within and between observations (e.g. the middle two panels of Fig. 3).

Period and Period Derivative We used phase dispersion minimization based on Lafler-Kinman statistic^{36–39} to quantify the periodicity of the pulses, using the package P4J (<https://github.com/phuijse/P4J>). This choice is motivated by the variable shape and amplitude of the pulses and presence of large irregular gaps in data (which occasionally truncate part of an observed pulse). Using this method we found a clear peak in the periodogram with a period of 1091.170 s.

The period obtained from the periodogram analysis above assumes that the period is constant (i.e. $\dot{P} = 0$). In order to place constraints on \dot{P} , we performed a grid search of P and \dot{P} values, centred on 1091.170 s and 0 s s^{-1} respectively, to find which pairs of values are consistent with the observed arrival times of the pulses. We searched over the ranges $1091.150 \text{ s} \leq P \leq 1091.185 \text{ s}$ and $-4 \times 10^{-9} \leq \dot{P} \leq 4 \times 10^{-9}$, aligning the pulses in pulse phase for each value pair, and taking the peak flux density of the averaged pulses (the “mean profile” in pulsar parlance) as our metric for goodness of alignment. Since different pulses were observed in different frequency bands, each brought to a common frequency of 154 MHz using $\alpha = -1.16$ (see below), before averaging.

As shown in Extended Data Fig. 2, the resulting P and \dot{P} were somewhat degenerate, as expected due to the three-month time window of measurements and the evolving pulse profile. The maximum peak flux density 15.5 Jy corresponds to the values $P = 1091.1690 \pm 0.0005 \text{ s}$ and $\dot{P} = 6 \times 10^{-10} \text{ s s}^{-1}$. The most significant contour in Extended Data Fig. 2 is shown at 15 Jy to show that there are multiple values of P and \dot{P} which produce a similar flux density. Therefore, this analysis favours the ranges $0 < \dot{P} < 1.2 \times 10^{-9}$, i.e. spin-down is more likely than spin-up.

Note that the error on the source period is representative for any choice of \dot{P} within this range, reflecting the width of the most significant contour in the period dimension.

Spectral index Individual 30.72-MHz observations of GLEAM-X J 162759.5-523504.3 lack the frequency coverage to determine an accurate spectral index, but since the flux density clearly varies with time, averaging over many observations is unlikely to yield a usable result. To obtain a good estimate, we used the same observations with which we measured the dispersion measure: 1205008192 (72–103 MHz), 1205007112 (103–134 MHz), 1205011432 (139–170 MHz), 1205010352 (170–200 MHz), and 1205009272 (200–231 MHz); these are the observations taken on 2018-03-13 between 20:12 and 21:24 (Fig. 1), where the pulse profile is reasonably consistent with time. After dedispersion and alignment on the source period, we obtained an average profile by averaging the data along the combined frequency axis (vertical axis in the right-hand panel of Extended Data Fig. 1). From this we selected the timesteps where the source was clearly “on” (timesteps 0–100 in the right-hand panel of Extended Data Fig. 1), and for each frequency, determined the weighted average flux density, using the average profile as a weighting function.

Errors were calculated as the root-mean-squared noise of each slice for unflagged timesteps during which the source was “off”, divided by the square root of the number of samples in the average flux density measurement, added in quadrature with a 5% flux density calibration error. Extended Data Fig. 3 shows the weighted averages and their errors plotted as a function of frequency. The drop-off at low frequencies is likely due to averaging over the strong ionospheric scintillation (time-dependent striping visible in the top of Extended Data Fig. 1), while the steepening at the higher frequencies may be intrinsic, but the signal-to-noise is low so it is difficult to

be sure. Therefore, we used the measurements taken between 95 and 195 MHz and the `scipy` implementation of a the Levenberg-Marquardt least-squares fit to determine a radio spectral index of $\alpha = -1.16 \pm 0.04$, where the flux density $S_\nu \propto \nu^\alpha$. The reduced- χ^2 of the fit is 1.86.

Error on the distance estimate Models of the Galactic electron density can be used to convert the dispersion measure (DM) into a distance. YMW 2016, the most recent model⁵, derives a relative distance error $\frac{D_m - D_i}{D_i}$ using 189 pulsars for which distances are known: D_m is the model distance based on the observed DM and D_i is the independently determined distance (e.g. by parallax). For their sample, the root-mean-square of the relative distance error is 0.398. From version 1.65 of the Australia Telescope National Facility Pulsar Catalogue⁴⁰, we extracted data for the five pulsars with independently-measured distances within 10° of GLEAM-X J 162759.5-523504.3. For these pulsars, we found that the root-mean-square of the relative distance error is 0.393. Thus we conclude that there is a $\sim 40\%$ error on the estimated distance of 1.3 kpc.

Position measurement At radio frequencies, the apparent source position measured by an interferometer may be shifted by an angular offset $\Delta\theta$ by the ionosphere, proportional to the transverse gradient ∇_\perp of the total electron content (TEC) toward the source and the square of the wavelength at which the observations were taken. To determine an accurate position for GLEAM-X J 162759.5-523504.3, we used observation 1205009272, taken at the highest frequency band, 200 – 231 MHz, on a quiet night during which ionospheric distortions were minimised, and imaging just the 30-s subset of the observation during a high S/N pulse. We used the software `FITS_WARP`⁴¹ to calculate the local position shift based on the apparent shifts of nearby compact bright calibrator sources. The error was calculated as the mean residual offset of these nearby sources after the

shift had been modelled and removed, i.e. $2''$. The derived position is R.A. $16^{\text{h}}27^{\text{m}}59.5^{\text{s}}$, Dec. $-52^{\circ}35'04.3''$.

Swift/XRT Observations We observed GLEAM-X J 162759.5-523504.3 with the Neil Gehrels *Swift* observatory⁴² for 2 ks with the X-ray telescope (XRT)⁴³ in photon-counting mode. The observations were taken from 2021-02-25 16:34:00 to 2021-02-25 21:27:00 (UTC) and the observation id was 00014085001. We reduced and analyzed the data using HEASOFT v6.28⁴⁴, and the XRTPipeline v0.13.5. There is no detection of a point source in any bands, nor is there any indication of extended structure. We estimate a $3\text{-}\sigma$ upper limit of $5.6 \times 10^{-3} \text{ ct s}^{-1}$ for the count rate in the 0.3–10 keV band for GLEAM-X J 162759.5-523504.3. Assuming a thermal spectrum (blackbody, $kT = 0.1 \text{ keV}$), the upper limit in count rate corresponds to an absorbed flux of $1.5 \times 10^{-13} \text{ erg s}^{-1} \text{ cm}^{-2}$ in the 0.3–10 keV band. Assuming a non-thermal spectrum ($E^{-\alpha}$; $\alpha = 2$, typical for magnetars¹⁶), the upper limit in count rate corresponds to an absorbed flux of $1.9 \times 10^{-13} \text{ erg s}^{-1} \text{ cm}^{-2}$ in the 0.3–10 keV band. Extended Data Fig. 4 shows the corresponding luminosity limit calculated as a function of kT .

Radio luminosity calculation Working under the assumption that GLEAM-X J 162759.5-523504.3 is a pulsar or magnetar in order to determine its energetics, we can transform the observed flux density into a radio luminosity. To precisely determine the radio luminosity of a rotating magnetic neutron star its geometry with respect to the observer needs to be known; this is often derived by examining the change in pulse phase with respect to time. In the case of GLEAM-X J 162759.5-523504.3, the pulse phase is flat, similar to the case of the radio magnetar Swift J 1818.0 – 1607⁴⁵. In this case, we cannot derive the geometry of the emission cone and instead interpret the flat

phase as our line-of-sight just grazing the edge of the emission cone (i.e. the impact angle between the line-of-sight and the magnetic axis is similar to the emission cone opening angle). This is qualitatively consistent with the pulse duty cycle of 30–60 s of activity in 1091 s, $\approx 3\text{--}6\%$. For pulsars with this duty cycle, for typical opening angles of 6° , the radio luminosity at 1.4 GHz is⁴⁶ $7.4 \times 10^{30} \frac{D}{\text{kpc}}^2 \frac{S_{1.4\text{GHz}}}{\text{Jy}} \text{erg s}^{-1}$. GLEAM-X J 162759.5-523504.3 produces pulses of peak flux densities of up to $S_{154\text{MHz}} = 45 \text{ Jy}$. Scaling this to 1.4 GHz by $\alpha = -1.16$ we would expect $S_{1.4\text{GHz}} = 3.5 \text{ Jy}$, and therefore $L_{1.4\text{GHz}} = 4 \times 10^{31} \text{erg s}^{-1}$.

Long-term duty cycle In 8 years of operation, the MWA has accumulated ~ 160 hours of observing time that have pointing directions within 15° of GLEAM-X J 162759.5-523504.3, and might in principle be sensitive to it. However, since the data span many different projects, array configurations, frequencies, and observing modes, and processing data takes about $100\times$ longer than observing, searching this data thoroughly is a daunting task. Additionally, only when the data are taken in a contiguous ~ 20 -minute block may emission from this source be ruled out. We first examined the data before the 2018-Jan – Mar activity window using the period of the source, and found no emission from GLEAM-X J 162759.5-523504.3 in 2017-Dec or 2018-Apr. We searched five blocks of 20-minute contiguous observations in 2017-May, 2017-Oct, 2017-Nov, 2018-Apr, 2018-May, finding no detections. Before 2017-May and after 2018-Jun, the telescope was re-configured into compact “Hex” mode, a redundant-baseline configuration with very poor imaging quality, yielding poor constraints from data taken in that mode. We searched for suitable observations in the archive as early as possible (2014-Mar and 2014-Jun), and also took new observations (2021-Feb), finding no detections. There remains in the archive ~ 15 hours of data in suitable

contiguous 20-minute blocks that may be searched in a future paper.

At the time of writing, the MWA has been in operation for 8 years, and this source was only found to be active for 2 months in that time, yielding an estimate of the duty cycle of $\frac{60 \text{ days active}}{3000 \text{ days searched}} = 2\%$. Alternatively, we could assume that the source was active any time that we have not thoroughly searched the data, and with the co-operation of a conspiratorial Universe, the duty cycle can trend toward 100%. Or, this might be the only time in the (unknown) lifetime of the source that it has produced emission, resulting in a duty cycle trending toward 0%. It is also worth noting that the source may not be entirely inactive during our non-detections, but its pulsations may be below our detection threshold; follow-up with a more sensitive radio telescope would be illuminating. For this work, we use the estimate of a 2% long-term duty cycle for pulses above the detection threshold of the MWA.

Pulse profile evolution and alignment At first examination, the three pulses recorded on Jan 03 appear to be misaligned with the other pulses. However, the pulses recorded on Mar 13 show an early “secondary” pulse preceeding the main pulse by ~ 15 s. Aligned by our determined P and \dot{P} , the pulses from Jan 03 fit within the wide pulse profiles found in Mar 13 (Extended Data Fig. 5). We therefore suggest that there is no misalignment, and instead the apparent effect is caused by pulse profile evolution.

25. Tingay, S. J. *et al.* The Murchison Widefield Array: The Square Kilometre Array Precursor at Low Radio Frequencies. *Publ. Astron. Soc. Aust.* **30**, 7 (2013).
26. Wayth, R. B. *et al.* The Phase II Murchison Widefield Array: Design overview. *Publ. Astron.*

- Soc. Aust.* **35**, 33 (2018).
27. Wayth, R. B. *et al.* GLEAM: The GaLactic and Extragalactic All-Sky MWA Survey. *Publ. Astron. Soc. Aust.* **32**, e025 (2015).
 28. Offringa, A. R. *et al.* Parametrizing Epoch of Reionization foregrounds: a deep survey of low-frequency point-source spectra with the Murchison Widefield Array. *Mon. Not. R. Astron. Soc.* **458**, 1057–1070 (2016).
 29. Hurley-Walker, N. *et al.* GaLactic and Extragalactic All-sky Murchison Widefield Array (GLEAM) survey II: Galactic plane $345^\circ \leq l \leq 67^\circ$, $180^\circ \leq b \leq 240^\circ$. *Publ. Astron. Soc. Aust.* **36**, e047 (2019).
 30. Offringa, A. R. *et al.* WSCLEAN: an implementation of a fast, generic wide-field imager for radio astronomy. *Mon. Not. R. Astron. Soc.* **444**, 606–619 (2014).
 31. Sutunjo, A. *et al.* Understanding instrumental Stokes leakage in Murchison Widefield Array polarimetry. *Radio Sci.* **50**, 52–65 (2015).
 32. Lenc, E. *et al.* The Challenges of Low-Frequency Radio Polarimetry: Lessons from the Murchison Widefield Array. *Publ. Astron. Soc. Aust.* **34**, e040 (2017).
 33. Riseley, C. J. *et al.* The POLarised GLEAM Survey (POGS) I: First results from a low-frequency radio linear polarisation survey of the southern sky. *Publ. Astron. Soc. Aust.* **35**, 43 (2018).

34. Riseley, C. J. *et al.* The POLarised GLEAM Survey (POGS) II: Results from an all-sky rotation measure synthesis survey at long wavelengths. *Publ. Astron. Soc. Aust.* **37**, e029 (2020).
35. Brentjens, M. A. & De Bruyn, A. Faraday rotation measure synthesis. *Astronomy & Astrophysics* **441**, 1217–1228 (2005).
36. Lafler, J. & Kinman, T. D. An RR Lyrae Star Survey with the Lick 20-INCH Astrograph II. The Calculation of RR Lyrae Periods by Electronic Computer. *Astrophys. J. Suppl.* **11**, 216 (1965).
37. Stellingwerf, R. F. Period determination using phase dispersion minimization. *Astrophys. J.* **224**, 953–960 (1978).
38. Schwarzenberg-Czerny, A. Fast and Statistically Optimal Period Search in Uneven Sampled Observations. *Astrophys. J. Lett.* **460**, L107 (1996).
39. Clarke, D. String/Rope length methods using the Lafler-Kinman statistic. *Astron. & Astrophys.* **386**, 763–774 (2002).
40. Manchester, R. N., Hobbs, G. B., Teoh, A. & Hobbs, M. The Australia Telescope National Facility Pulsar Catalogue. *Astron. J.* **129**, 1993–2006 (2005).
41. Hurley-Walker, N. & Hancock, P. J. De-distorting ionospheric effects in the image plane. *Astron. Comput.* **25**, 94–102 (2018).
42. Gehrels, N. *et al.* The Swift Gamma-Ray Burst Mission. *Astrophys. J.* **611**, 1005–1020 (2004).
43. Burrows, D. N. *et al.* The Swift X-Ray Telescope. *Space Sci. Rev.* **120**, 165–195 (2005).

44. Nasa High Energy Astrophysics Science Archive Research Center (Heasarc). HEASoft: Unified Release of FTOOLS and XANADU (2014).
45. Champion, D. *et al.* High-cadence observations and variable spin behaviour of magnetar Swift J1818.0-1607 after its outburst. *Mon. Not. R. Astron. Soc.* **498**, 6044–6056 (2020).
46. Lorimer, D. R. & Kramer, M. *Handbook of Pulsar Astronomy* (Cambridge University Press, 2012).
47. Zhang, B., Harding, A. K. & Muslimov, A. G. Radio Pulsar Death Line Revisited: Is PSR J2144-3933 Anomalous? *Astrophys. J. Lett.* **531**, L135–L138 (2000).

Acknowledgements N.H.-W. is the recipient of an Australian Research Council Future Fellowship (project number FT190100231) and G.E.A. is the recipient of an Australian Research Council Discovery Early Career Researcher Award (project number DE180100346) funded by the Australian Government. This scientific work makes use of the Murchison Radio-astronomy Observatory, operated by CSIRO. We acknowledge the Wajarri Yamatji people as the traditional owners of the Observatory site. Support for the operation of the MWA is provided by the Australian Government (NCRIS), under a contract to Curtin University administered by Astronomy Australia Limited. We acknowledge the Pawsey Supercomputing Centre which is supported by the Western Australian and Australian Governments. The National Radio Astronomy Observatory is a facility of the National Science Foundation operated under cooperative agreement by Associated Universities, Inc. This project was supported by resources and expertise provided by CSIRO IMT Scientific Computing. This work used resources of China SKA Regional Centre prototype funded by the National Key R&D Programme of China (2018YFA0404603) and Chinese Academy of Sciences (114231KYSB20170003).

Author Contributions N.H.-W. calibrated and processed the data for the observations described herein, determined the position and flux density of the source, and prepared the manuscript with contributions from all co-authors. X.Z. processed all polarization data, including performing polarization calibration and analysis. A.B. and S.J.M. performed the analysis to derive the period and period derivative. A.B. performed the X-ray observations and analysis. S.J.M. calculated and applied the dispersion measure and barycentric corrections. T.N.O. developed the original detection methodology, performed the original archive search, and made the initial discovery. P.J.H. helped develop the detection methodology and provided super-computing support. G.E.A. contributed to astrophysical calculations and interpretation of the data. T.J.G., G.H.H., J.S.M., and X.Z. determined polarization calibration methods. T.J.G. performed early refinement of the period estimate.

Competing Interests The authors declare that they have no competing financial interests.

Data Availability Data that supports this paper are available at the following public repository:

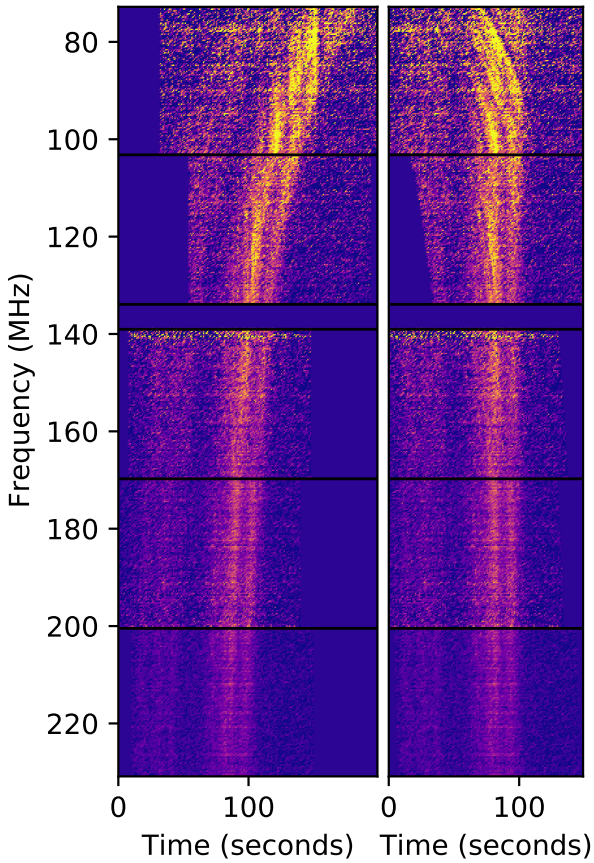
https://github.com/nhurleywalker/GLEAM-X_Periodic_Transient. Further data products can be supplied by the authors on reasonable request.

Code Availability Code that supports this paper is available at the following public repository:

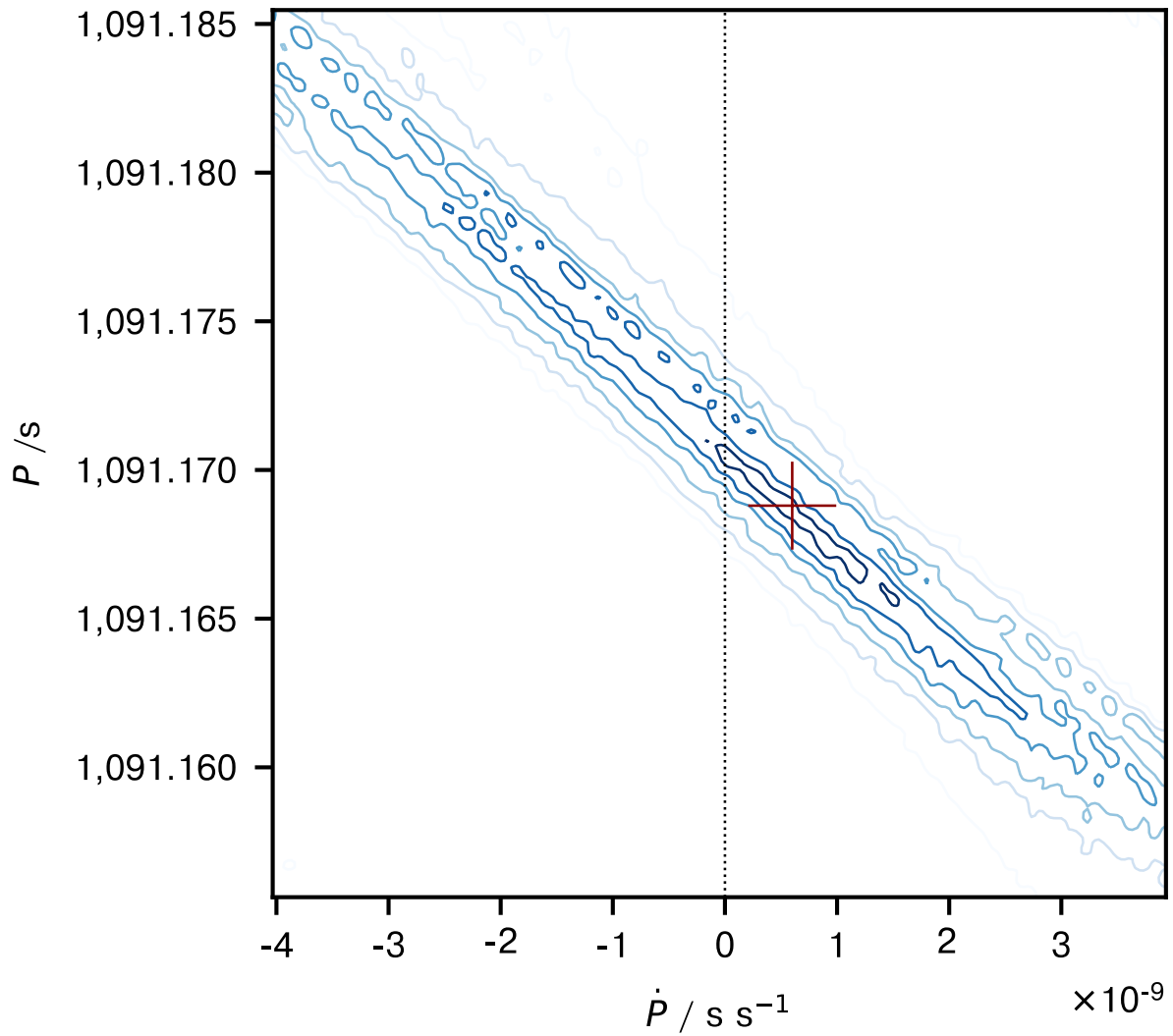
https://github.com/nhurleywalker/GLEAM-X_Periodic_Transient. Fig. 4 was generated using https://github.com/nhurleywalker/Transient_Phase_Space. Further code can be supplied by the authors on reasonable request.

Correspondence Correspondence and requests for materials should be addressed to N.H.-W. (nhw@icrar.org)

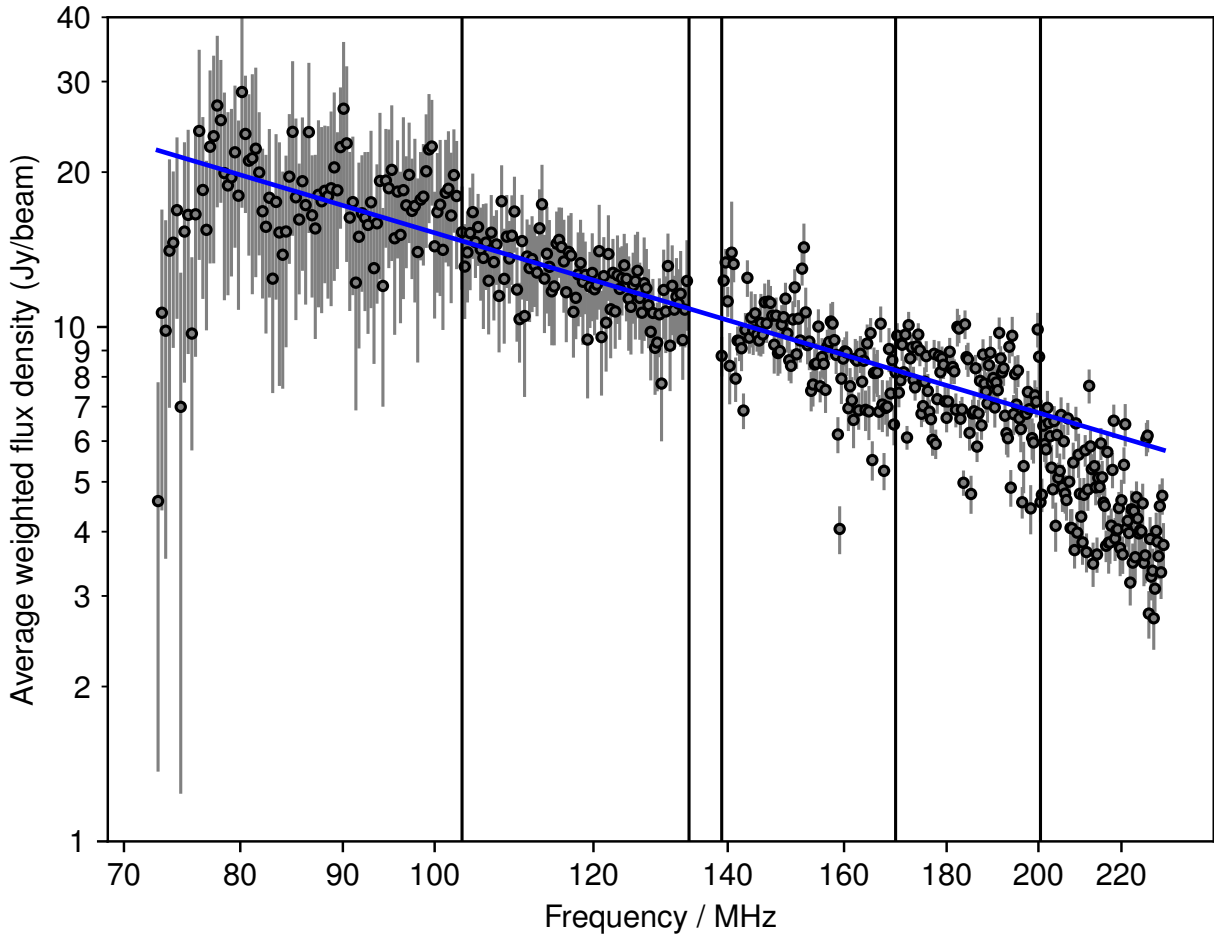
Extended Data



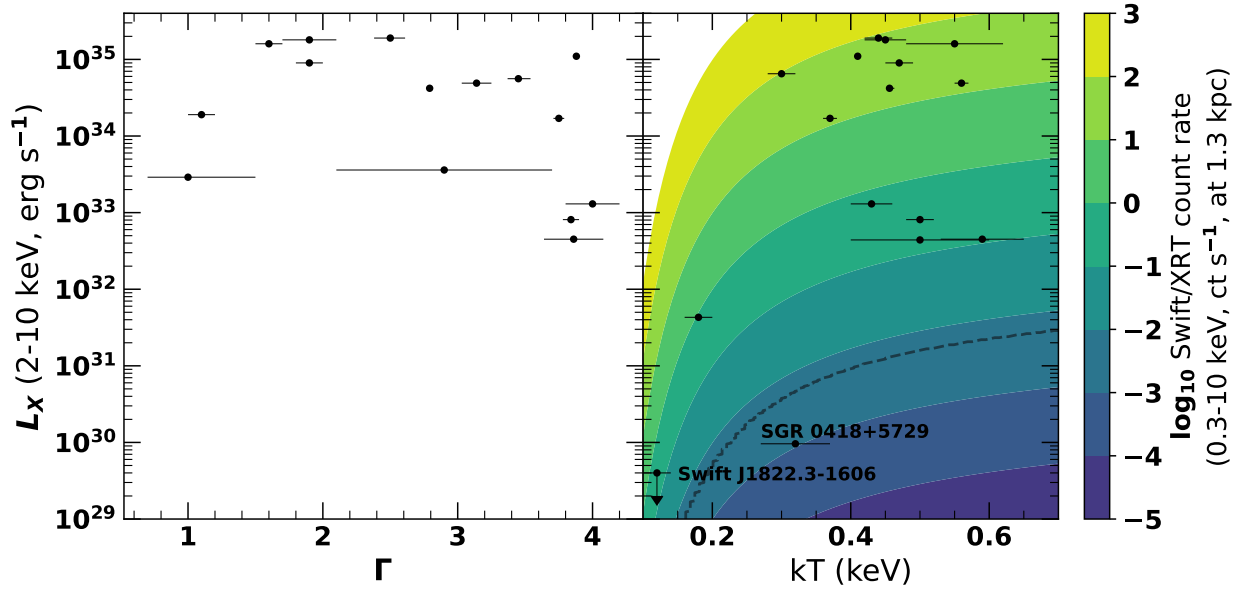
Extended Data Figure 1: Dynamic spectra of the observations used to measure the dispersion measure. From top to bottom, separated by horizontal black lines we show the observations 1205008192 (72–103 MHz), 1205007112 (103–134 MHz), 1205011432 (139–170 MHz), 1205010352 (170–200 MHz), and 1205009272 (200–231 MHz). These observations were taken on 2018-03-13 between 20:12 and 21:24 (see Fig. 1). The left panel shows the data aligned using a period of 1091.1690 s, while the right panel shows the same, including a dispersion correction of 57 pc cm^{-3} . Strong ionospheric scintillation is visible in the 72–103 MHz data, causing ripples in the brightness of the source over time.



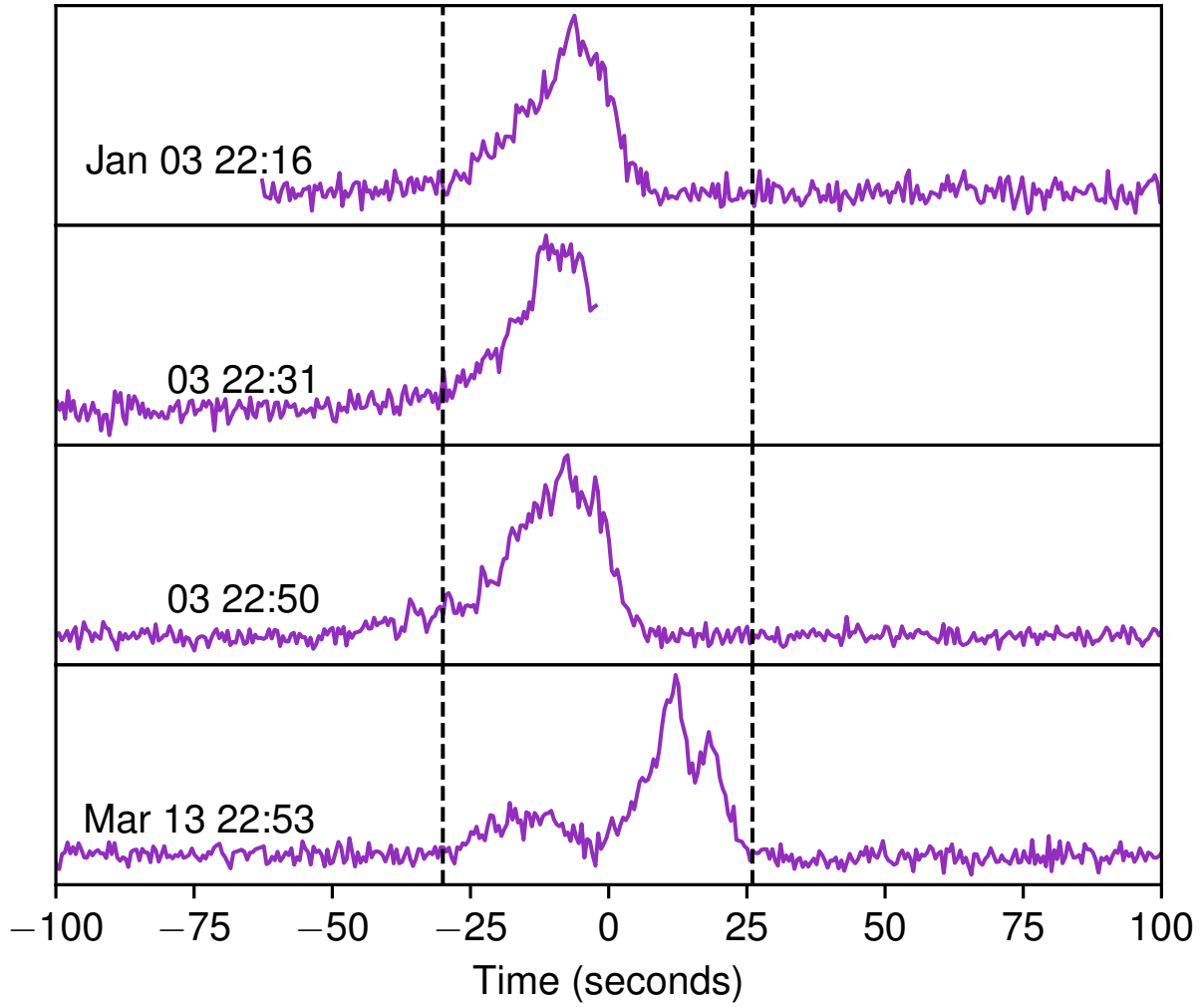
Extended Data Figure 2: The explored search space in P and \dot{P} for the pulses recorded from GLEAM-X J162759.5-523504.3. The contours show the peak flux density of the mean profile at 154 MHz recovered at each combination of P (vertical axis) and \dot{P} (horizontal axis), in levels of 15, 14, 13, 12, and 11 Jy. The best-fit values of $P = 1091.1690$ s and $\dot{P} = 6 \times 10^{-10}$ s s^{-1} are marked with a dark red “+”.



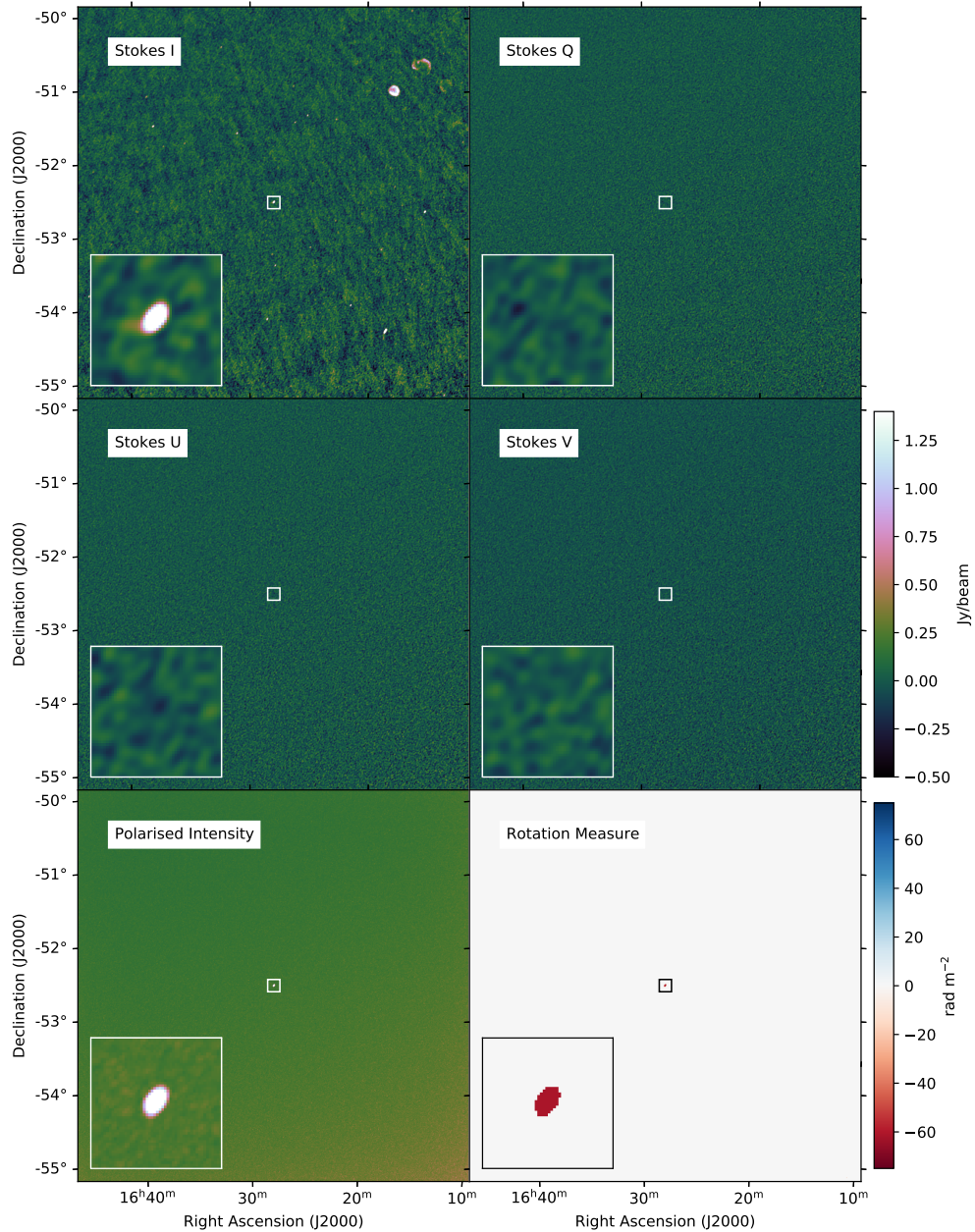
Extended Data Figure 3: The flux density of GLEAM-X J162759.5-523504.3 as a function of frequency. This is derived from the same observations shown in Extended Data Fig. 1. Points are determined via an average of the source profile in each frequency bin, weighting by the signal-to-noise of the frequency-averaged profile. A power-law fit using the data spanning 95–195 MHz is shown in blue, with $\alpha = -1.16 \pm 0.04$.



Extended Data Figure 4: X-ray luminosity and spectral properties of magnetars¹⁶ compared to the X-ray luminosity limits of GLEAM-X J 162759.5-523504.3. The two faintest known magnetars are labelled. The colored contours represent expected *Swift*/XRT count rates for putative X-ray luminosities and blackbody temperatures for a source at 1.3 kpc, assuming a hydrogen column density of $N_{\text{H}} \approx 2 \times 10^{21} \text{ cm}^{-2}$. The gray dashed line represents the implied luminosity upper limit for GLEAM-X J 162759.5-523504.3 based on the $3\text{-}\sigma$ upper limit obtained from the *Swift*/XRT observation. From the magnetar fundamental plane, we predict GLEAM-X J 162759.5-523504.3 to have a quiescent luminosity 4.5 orders of magnitude lower than our limit from *Swift*/XRT.



Extended Data Figure 5: Pulse profiles for the three detections on Jan 03, compared with a wide pulse detected on Mar 14. Barycentric corrections and dedispersion have been applied. The data are all taken at the same frequency, 170–200 MHz. Vertical dashed lines encapsulating the profile found on Mar 13 are overplotted to guide the eye.

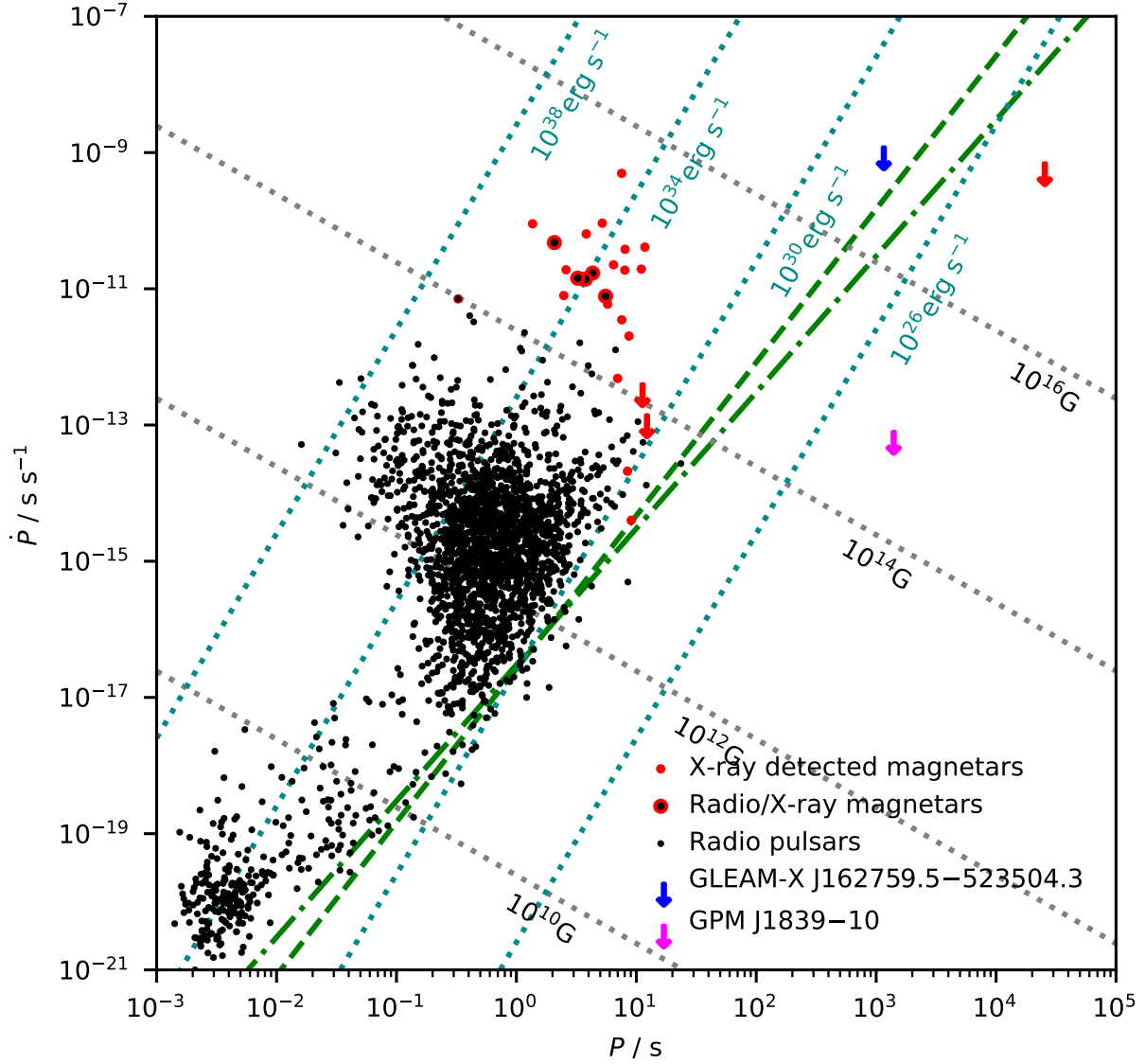


Extended Data Figure 6: Images in full Stokes and polarised intensity (in Jy beam^{-1}), and rotation measure (in rad m^{-2}), of the region $5^\circ \times 5^\circ$ around GLEAM-X J 162759.5-523504.3. The images were made using observation 1200354592 at 2018-01-18T23:49, using only the interval where the source was producing emission. Faraday rotation over the imaged bandwidth of 30 MHz causes the Stokes Q, U, and V emission to average to zero. The polarised intensity shows the maximum value of the Rotation Measure spectrum. Where the polarised intensity is $< 7\times$ the local noise, the corresponding RM value has been masked.

Methods

Observations The Murchison Widefield Array is a low-frequency radio telescope operating in the Murchison region of Western Australia^{25,26}. At the time of the observation in which GLEAM-X J 162759.5-523504.3 was discovered, it was engaged in observing the GaLactic and Extragalactic All-sky MWA – eXtended (GLEAM-X) survey, a follow-up to the GLEAM survey²⁷. The data were taken in a drift scan mode, iterating through a 72–231 MHz bandwidth by dwelling for 2 minutes in each of five 30.72-MHz bands, yielding a resolution of $5'–45''$ and snapshot noise levels of $150–25$ mJy beam⁻¹. Over this bandwidth the field-of-view of the instrument is $60^\circ–25^\circ$ across, yielding multiple measurements of sources drifting through the primary beam. The data are sampled at 0.5-s time resolution and 10-kHz frequency resolution. We downloaded measurement sets from the MWA All-Sky Virtual Observatory (<https://asvo.mwatelescope.org/>) and at this stage averaged the data to 40 kHz to reduce data size and decrease processing times.

The initial detection of the transient was made by performing a differencing of the visibilities between observations taken at an identical Local Sidereal Time several months apart (Hancock et al. in prep). Two detections were made, and based on the non-detections in adjacent observations, an initial period was determined. Including a barycentric correction, and searching the archive thoroughly between July 2017 and July 2018, the interval of activity was established to be January 2018 to March 2018, with a total of 71 detections (see Supplementary Methods for further details on searching the MWA archive).



Extended Data Figure 7: A scatter plot of period derivative \dot{P} against period P . GLEAM-X J 162759.5-523504.3 is shown as a blue arrow with an upper limit on \dot{P} (see Methods) in context with the known pulsars⁴⁰ (black dots), X-ray-detected magnetars¹⁶ (red dots and arrows), and magnetars known to emit in both X-ray and radio (red circles around black dots). The slowest (and radio-quiet) X-ray magnetar 1E 161348–5055 is also shown with an upper limit on \dot{P} . The green dashed and dot-dashed lines correspond to the theoretical “death lines” for pulsar radio emission for cases I and III calculated by Zhang et al.⁴⁷.

Calibration and imaging For all data, calibration was performed using the MITHCAL algorithm²⁸ to derive antenna gains by comparing the raw data to model visibilities formed from a sky model based on catalogues derived from GLEAM^{24,29}. These were applied to the observation, and deep imaging was subsequently performed using WSCLEAN³⁰ version 2.9.0, creating a visibility model that includes the spectrally variant primary beam. A $10' \times 10'$ region around GLEAM-X J 162759.5-523504.3 was masked during this process, so that the source is not included in the model.

After the deep model was created and subtracted from the visibilities, the data were re-imaged such that the transient was the only source in the field. The data were imaged at 320 kHz frequency resolution and 0.5 s time resolution in full Stokes (I,Q,U,V), which were formed from the instrumental data by application of the MWA beam model³¹. We also used observations of a polarisation calibrator (PKS J0636–2036) to correct radio emission leaking from Stokes U into Stokes V (X-Y phase calibration³²).

Dispersion Measure Since strong pulse profile evolution is observed, we used the five observations that spanned 72–231 MHz in the shortest interval of time (74 minutes; Extended Data Fig. 1) to calculate the dispersion measure. We aligned these observations using a period of 1091.1690 s, then ran dedispersion trials in steps of 0.5 over range 50 to 60 pc cm^{-3} , finding that $57 \pm 1 \text{ pc cm}^{-3}$ produced the best fit. Light curves (Fig. 2) were then produced for each observation by applying dedispersion and averaging the dynamic spectra along the frequency axis.

Polarisation Polarisation analysis was performed following the methods of the POLarised GLEAM Survey (POGS^{33,34}). From all observations with detections, only observations within 170–230

MHz were selected for the polarisation analysis to avoid depolarisation caused by the (40 kHz) channel width. We performed RM synthesis³⁵ on the time-averaged Q/U spectrum of each observation with the RM Tools software (<https://github.com/CIRADA-Tools/RM-Tools>) to obtain the corresponding RM, fractional polarisation, and polarisation angle. To investigate any variation of the polarisation angle within the pulse phase, we also performed RM synthesis on the Q/U spectrum of each timestep for two high S/N observations. We found that the polarisation angle was constant with respect to time within and between observations (e.g. the middle two panels of Fig. 3).

Period and Period Derivative We used phase dispersion minimization based on Lafler-Kinman statistic^{36–39} to quantify the periodicity of the pulses, using the package P4J¹. This choice is motivated by the variable shape and amplitude of the pulses and presence of large irregular gaps in data (which occasionally truncate part of an observed pulse). Using this method we found a clear peak in the periodogram with a period of 1091.170 s.

The period obtained from the periodogram analysis above assumes that the period is constant (i.e. $\dot{P} = 0$). In order to place constraints on \dot{P} , we performed a grid search of P and \dot{P} values, centred on 1091.170 s and 0 s s^{-1} respectively, to find which pairs of values are consistent with the observed arrival times of the pulses. We searched over the ranges $1091.150 \text{ s} \leq P \leq 1091.185 \text{ s}$ and $-4 \times 10^{-9} \leq \dot{P} \leq 4 \times 10^{-9}$, aligning the pulses in pulse phase for each value pair, and taking the peak flux density of the averaged pulses (the “mean profile” in pulsar parlance) as our metric for goodness of alignment. Since different pulses were observed in different frequency bands, each

¹<https://github.com/phuijse/P4J>

brought to a common frequency of 154 MHz using $\alpha = -1.16$ (see below), before averaging.

As shown in Extended Data Fig. 2, the resulting P and \dot{P} were somewhat degenerate, as expected due to the three-month time window of measurements and the evolving pulse profile. The maximum peak flux density 15.5 Jy corresponds to the values $P = 1091.1690 \pm 0.0005$ s and $\dot{P} = 6 \times 10^{-10} \text{ s s}^{-1}$. The most significant contour in Extended Data Fig. 2 is shown at 15 Jy to show that there are multiple values of P and \dot{P} which produce a similar flux density. Therefore, this analysis favours the ranges $0 < \dot{P} < 1.2 \times 10^{-9}$, i.e. spin-down is more likely than spin-up. Note that the error on the source period is representative for any choice of \dot{P} within this range, reflecting the width of the most significant contour in the period dimension.

Spectral index Individual 30.72-MHz observations of GLEAM-X J 162759.5-523504.3 lack the frequency coverage to determine an accurate spectral index, but since the flux density clearly varies with time, averaging over many observations is unlikely to yield a usable result. To obtain a good estimate, we used the same observations with which we measured the dispersion measure: 1205008192 (72–103 MHz), 1205007112 (103–134 MHz), 1205011432 (139–170 MHz), 1205010352 (170–200 MHz), and 1205009272 (200–231 MHz); these are the observations taken on 2018-03-13 between 20:12 and 21:24 (Fig. 2), where the pulse profile is reasonably consistent with time. After dedispersion and alignment on the source period, we obtained an average profile by averaging the data along the combined frequency axis (vertical axis in the right-hand panel of Extended Data Fig. 1). From this we selected the timesteps where the source was clearly “on” (timesteps 0–100 in the right-hand panel of Extended Data Fig. 1), and for each frequency, determined the weighted average flux density, using the average profile as a weighting function.

Errors were calculated as the root-mean-squared noise of each slice for unflagged timesteps during which the source was “off”, divided by the square root of the number of samples in the average flux density measurement, added in quadrature with a 5 % flux density calibration error. Extended Data Fig. 3 shows the weighted averages and their errors plotted as a function of frequency. The drop-off at low frequencies is likely due to averaging over the strong ionospheric scintillation (time-dependent striping visible in the top of Extended Data Fig. 1), while the steepening at the higher frequencies may be intrinsic, but the signal-to-noise is low so it is difficult to be sure. Therefore, we used the measurements taken between 95 and 195 MHz and the `scipy` implementation of a the Levenberg-Marquardt least-squares fit to determine a radio spectral index of $\alpha = -1.16 \pm 0.04$, where the flux density $S_\nu \propto \nu^\alpha$. The reduced- χ^2 of the fit is 1.86.

Error on the distance estimate Models of the Galactic electron density can be used to convert the dispersion measure (DM) into a distance. YMW 2016, the most recent model⁵, derives a relative distance error $\frac{D_m - D_i}{D_i}$ using 189 pulsars for which distances are known: D_m is the model distance based on the observed DM and D_i is the independently determined distance (e.g. by parallax). For their sample, the root-mean-square of the relative distance error is 0.398. From version 1.65 of the Australia Telescope National Facility Pulsar Catalogue⁴⁰, we extracted data for the five pulsars with independently-measured distances within 10° of GLEAM-X J 162759.5-523504.3. For these pulsars, we found that the root-mean-square of the relative distance error is 0.393. Thus we conclude that there is a $\sim 40\%$ error on the estimated distance of 1.3 kpc.

Position measurement At radio frequencies, the apparent source position measured by an interferometer may be shifted by an angular offset $\Delta\theta$ by the ionosphere, proportional to the trans-

verse gradient ∇_{\perp} of the total electron content (TEC) toward the source and the square of the wavelength at which the observations were taken. To determine an accurate position for GLEAM-X J 162759.5-523504.3, we used observation 1205009272, taken at the highest frequency band, 200 – 231 MHz, on a quiet night during which ionospheric distortions were minimised, and imaging just the 30-s subset of the observation during a high S/N pulse. We used the software FITS_WARP⁴¹ to calculate the local position shift based on the apparent shifts of nearby compact bright calibrator sources. The error was calculated as the mean residual offset of these nearby sources after the shift had been modelled and removed, i.e. $2''$. The derived position is R.A. $16^{\text{h}}27^{\text{m}}59.5^{\text{s}}$, Dec. $-52^{\circ}35'04.3''$.

Swift/XRT Observations We observed GLEAM-X J 162759.5-523504.3 with the Neil Gehrels *Swift* observatory⁴² for 2 ks with the X-ray telescope (XRT)⁴³ in photon-counting mode. The observations were taken from 2021-02-25 16:34:00 to 2021-02-25 21:27:00 (UTC) and the observation id was 00014085001. We reduced and analyzed the data using HEASOFT v6.28⁴⁴, and the XRTPIPELINE v0.13.5. There is no detection of a point source in any bands, nor is there any indication of extended structure. We estimate a $3-\sigma$ upper limit of $5.6 \times 10^{-3} \text{ ct s}^{-1}$ for the count rate in the 0.3–10 keV band for GLEAM-X J 162759.5-523504.3. Assuming a thermal spectrum (blackbody, $kT = 0.1 \text{ keV}$), the upper limit in count rate corresponds to an absorbed flux of $1.5 \times 10^{-13} \text{ erg s}^{-1} \text{ cm}^{-2}$ in the 0.3–10 keV band. Assuming a non-thermal spectrum ($E^{-\alpha}$; $\alpha = 2$, typical for magnetars¹⁶), the upper limit in count rate corresponds to an absorbed flux of $1.9 \times 10^{-13} \text{ erg s}^{-1} \text{ cm}^{-2}$ in the 0.3–10 keV band. Extended Data Fig. 4 shows the corresponding luminosity limit calculated as a function of kT .

Radio luminosity calculation Working under the assumption that GLEAM-X J 162759.5-523504.3 is a pulsar or magnetar in order to determine its energetics, we can transform the observed flux density into a radio luminosity. To precisely determine the radio luminosity of a rotating magnetic neutron star its geometry with respect to the observer needs to be known; this is often derived by examining the change in pulse phase with respect to time. In the case of GLEAM-X J 162759.5-523504.3, the pulse phase is flat, similar to the case of the radio magnetar Swift J 1818.0 – 1607⁴⁵. In this case, we cannot derive the geometry of the emission cone and instead interpret the flat phase as our line-of-sight just grazing the edge of the emission cone (i.e. the impact angle between the line-of-sight and the magnetic axis is similar to the emission cone opening angle). This is qualitatively consistent with the pulse duty cycle of 30–60 s of activity in 1091 s, $\approx 3\text{--}6\%$. For pulsars with this duty cycle, for typical opening angles of 6° , the radio luminosity at 1.4 GHz is⁴⁶ $7.4 \times 10^{30} \frac{D}{\text{kpc}}^2 \frac{S_{1.4\text{GHz}}}{\text{Jy}} \text{erg s}^{-1}$. GLEAM-X J 162759.5-523504.3 produces pulses of peak flux densities of up to $S_{154\text{MHz}} = 45 \text{ Jy}$. Scaling this to 1.4 GHz by $\alpha = -1.16$ we would expect $S_{1.4\text{GHz}} = 3.5 \text{ Jy}$, and therefore $L_{1.4\text{GHz}} = 4 \times 10^{31} \text{erg s}^{-1}$.

Long-term duty cycle In 8 years of operation, the MWA has accumulated ~ 160 hours of observing time that have pointing directions within 15° of GLEAM-X J 162759.5-523504.3, and might in principle be sensitive to it. However, since the data span many different projects, array configurations, frequencies, and observing modes, and processing data takes about $100\times$ longer than observing, searching this data thoroughly is a daunting task. Additionally, only when the data are taken in a contiguous ~ 20 -minute block may emission from this source be ruled out. We first examined the data before the 2018-Jan – Mar activity window using the period of the source, and

found no emission from GLEAM-XJ 162759.5-523504.3 in 2017-Dec or 2018-Apr. We searched five blocks of 20-minute contiguous observations in 2017-May, 2017-Oct, 2017-Nov, 2018-Apr, 2018-May, finding no detections. Before 2017-May and after 2018-Jun, the telescope was re-configured into compact “Hex” mode, a redundant-baseline configuration with very poor imaging quality, yielding poor constraints from data taken in that mode. We searched for suitable observations in the archive as early as possible (2014-Mar and 2014-Jun), and also took new observations (2021-Feb), finding no detections. There remains in the archive ~ 15 hours of data in suitable contiguous 20-minute blocks that may be searched in a future paper.

At the time of writing, the MWA has been in operation for 8 years, and this source was only found to be active for 2 months in that time, yielding an estimate of the duty cycle of $\frac{60 \text{ days active}}{3000 \text{ days searched}} = 2\%$. Alternatively, we could assume that the source was active any time that we have not thoroughly searched the data, and with the co-operation of a conspiratorial Universe, the duty cycle can trend toward 100%. Or, this might be the only time in the (unknown) lifetime of the source that it has produced emission, resulting in a duty cycle trending toward 0%. It is also worth noting that the source may not be entirely inactive during our non-detections, but its pulsations may be below our detection threshold; follow-up with a more sensitive radio telescope would be illuminating. For this work, we use the estimate of a 2% long-term duty cycle for pulses above the detection threshold of the MWA.

Pulse profile evolution and alignment At first examination, the three pulses recorded on Jan 03 appear to be misaligned with the other pulses. However, the pulses recorded on Mar 13 show an early “secondary” pulse preceding the main pulse by ~ 15 s. Aligned by our determined P and \dot{P} ,

the pulses from Jan 03 fit within the wide pulse profiles found in Mar 13 (Extended Data Fig. 5). We therefore suggest that there is no misalignment, and instead the apparent effect is caused by pulse profile evolution.